Fall 2014

Finite element modeling of trabecular bone from multi-row detector CT imaging

Cheng Chen
University of Iowa

FINITE ELEMENT MODELING OF TRABECULAR BONE FROM MULTI-ROW DETECTOR CT IMAGING

by

Cheng Chen

A thesis submitted in partial fulfillment of the requirements
for the Master of Science degree in Electrical and Computer Engineering
in the Graduate College of The University of Iowa

December 2014

Thesis Supervisor: Professor Punam K. Saha

Graduate College
The University of Iowa
Iowa City, Iowa

CERTIFICATE OF APPROVAL

_____

MASTER'S THESIS

_____

This is to certify that the Master's thesis of

Cheng Chen

has been approved by the Examining Committee
for the thesis requirement for the Master of Science
degree in Electrical and Computer Engineering at the December 2014 graduation.

Thesis Committee: _____
Punam K. Saha, Thesis Supervisor

_____
Nicole M. Grosland

_____
Hans J. Johnson

ACKNOWLEDGMENTS

First of all, I would like to give my most sincere thanks to my advisor Professor Punam K. Saha for his patient help and guidance on my research. I would like to thank Professor Nicole M. Grosland and Professor Hans J. Johnson working as my committee members. Also I would like to give my thanks to my colleagues Yinxiao Liu, Ziyue Xu, Dakai Jin, and Ryan Amelon for their help on my research. In the end, I want to thank all the faculty, staff and students of The Iowa Institute for Biomedical Imaging and Electrical and Computer Engineering for their improving lectures and kind help.

ABSTRACT

The finite element method (FEM) has been widely applied to various medical imaging applications over the past two decades. The remarkable progress in high-resolution imaging techniques has allowed FEM to draw great research interests in computing trabecular bone (TB) stiffness from three-dimensional volumetric imaging. However, only a few results are available in literature on applying FEM to multi-row detector CT (MDCT) imaging due to the challenges posed by limited spatial resolution. The research presented here develops new methods to preserve TB structure connectivity and to generate high-quality mesh representation for FEM from relatively low resolution images available at MDCT imaging. Specifically, it introduced a space-variant hysteresis algorithm to threshold local trabecular structure that preserves structure connectivity. Also, mesh generation algorithms was applied to represent TB micro-architecture and mesh quality was compared with that generated by traditional methods. TB stiffness was computed using FEM simulation on micro-CT (μ-CT) and MDCT images of twenty two cadaveric specimens of distal tibia. Actual stiffness of those specimens were experimentally determined by mechanical testing and its correlation with computed stiffness was analyzed. The observed values of linear correlation (r^2) between actual bone stiffness and computed stiffness from μ-CT and MDCT imaging were 0.95 and 0.88, respectively. Also, reproducibility of the FEM-based computed bone stiffness was determined from repeat MDCT scans of cadaveric specimens and the observed intra-class correlation coefficient was a high value of 0.98. Experimental results demonstrate the feasibility of application of FEM with high sensitivity and reproducibility on MDCT imaging of TB at distal tibia under in vivo condition.

PUBLIC ABSTRACT

Over the past two decades, trabecular bone (TB) study has drawn research interests to determine bone quality, understand causes of diseases, and assess risks of fractures. The finite element method (FEM) is an advanced computer-aided method that computes stiffness and simulates behaviors of target object. With the remarkable progress of high-resolution imaging techniques, FEM has been widely applied in TB study. However, only a few research focuses on FEM application on multi-row detector CT (MDCT) imaging because of limited spatial resolution. Since MDCT has advantages of fast acquisition, widely availability and capability of visualizing large bone structures, it has a great potential for clinical use. In this work, a framework of FEM modeling, which possesses several desired properties meeting requirements of FEM simulation, is presented and applied on MDCT and micro-CT (μ-CT). The framework introduces a space-variant hysteresis image processing method and applies state-of-the-art mesh generation algorithms to form an automatic system. Bone stiffness of TB is computed from twenty two cadaveric subjects using mechanical testing and FEM simulation on μ-CT and MDCT. Reproducibility of repeat MDCT scans was found to be 0.98. Linear correlations between mechanical testing and μ-CT, MDCT were found to be R^2 =0.95 and R^2 =0.88, respectively. The result demonstrates the feasibility and high sensitivity of the proposed framework. It is a fundamental tool for future studies of TB using MDCT imaging.

TABLE OF CONTENTS

LIST OF FIGURES

CHAPTER ONE

INTRODUCTION

1.1 Motivation and specific aims

Osteoporosis is a degenerative bone disease of high prevalence affecting older adults. The disorder is associated with high risk of low-trauma fractures leading to increased mortality and morbidity, and it entails significant healthcare costs. An estimated 8 million women and 2 million men in the United States meet the diagnostic criteria for osteoporosis (1). The percentage of patients with osteoporosis increases progressively with age – among US women, 13% in their 50s, 27% in their 60s, 47% in their 70s, and 67% in their 80s have bone density levels in the diagnostic range of osteoporosis (2). Clinically, osteoporosis is defined by low bone mineral density (BMD), which explains 65-75% of the variance in bone stiffness (3, 4), while the remaining variance is due to the cumulative and synergistic effects of various factors, including trabecular bone (TB) micro-architecture. There is evidence in the literature (5, 6) demonstrating that effects of therapeutic agents are greater on TB as compared to overall BMD. Results from several studies (6-12) support the hypothesis that quality of TB micro-architecture is an important determinant of bone stiffness and fracture risk.

Finite element method (FEM) has been widely applied to various medical imaging applications over the past two decades. The remarkable progress in high-resolution imaging techniques has allowed FEM to draw great research interests in computing trabecular bone (TB) stiffness from three-dimensional volumetric imaging. Ideally, the FEM provides a comprehensive assessment of the contribution of TB micro-architecture to bone stiffness. However, only a few results are available in literature on applying FEM to multi-row detector CT (MDCT) imaging due to the challenges posed by limited spatial resolution. The research presented here develops new methods to preserve the TB structural connectivity and to generate improved mesh representation for FEM from relatively low

resolution images available at MDCT imaging. The overall aim of this research is to develop a fully automated FEM-based algorithm to compute TB stiffness from MDCT imaging and to examine its sensitivity and reproducibility. This overall aim has been accomplished by completing the following individual aims.

Aim 1. Development of an automated FEM-based algorithm to compute TB stiffness from MDCT imaging.

a) Development of a space-variant hysteresis algorithm for thresholding local TB structure to preserve connectivity in MDCT images.

b) Application of surface mesh generation algorithm and volume mesh generation algorithm to represent TB micro-architecture with elements of good quality.

Aim 2. Examination of the sensitivity of FEM-based TB stiffness computation algorithm.

a) Collection of micro-CT (μ-CT) and MDCT images of twenty two cadaveric specimens of distal tibia.

b) Determination of actual stiffness of cadaveric specimens by mechanical testing.

c) Examination of the sensitivity of computed FEM-based bone stiffness by assessing its linear correlation with actual stiffness.

Aim 3. Examination of the reproducibility of FEM-based TB stiffness computation.

a) Collection of repeat scan MDCT images from cadavers and computation of FEM-based bone stiffness for all bone images.

b) Computation of intra-class correlation coefficient (ICC) of FEM-based bone stiffness measures from repeat scan images.

1.2 Finite element analysis on bone structure

In recent years, FEM has been widely used in the medical fields as a powerful tool to assess object stiffness, simulate material behaviors and understand structural properties. The complexity of TB micro-architecture makes it difficult to construct mathematical models. In literature, some measures are proposed (10, 13-15) to quantify structural properties of TB, based on topological and geometrical characteristics of TB network. However, FE

analysis of TB provides a model to assess TB micro-architecture, such as bone elastic property, material stiffness, fracture prediction, etc. (16, 17).

Over the past two decades, FEM has been widely applied on bone structural analysis together with increased spatial resolution in high-resolution bone imaging techniques, including magnetic resonance imaging (MRI), high resolution peripheral quantitative computed tomography (HRpQCT), μ-CT, and MDCT. Advanced bone imaging techniques provide high spatial resolution that enables researchers to build accurate FE models. Among these imaging modalities, μ-CT achieves the highest spatial resolution, but it is invasive to bone. In vivo imaging techniques, including MRI, HRpQCT and MDCT, attract more research attention because they are non-invasive and therefore suitable for clinical applications. In literature, various FE methods have been reported and applied on MRI (18), HRpQCT (19) and μ-CT (20). However, only a few results are available on MDCT (21, 22) due to the challenging image resolution. Compared with MRI and HRpQCT, MDCT has advantages of fast acquisition, widely availability and capability of visualizing large bone structures, which make it approprate for clinical use.

This work focused on FEM using MDCT images. It introduced a framework of FEM of MDCT images and evaluated reproducibility of bone stiffness with repeat MDCT images. It also demonstrated that bone stiffness generated by FEM was highly correlated to actual bone stiffness determined by mechanical testing.

1.3 Image processing and mesh generation

In computer aided design, FEM is applied on the mesh model of the object. The accuracy of FEM simulation depends on the quality of input surface and volume mesh, i.e., sizes and shapes of elements (23). A mesh of good quality provides accurate approximation of the target object, and a bad approximation reduces the reliability of the FE simulation. Good surface mesh preserves the true object surface with high quality elements. Good volume mesh generates elements with satisfactory size and shapes.

Generally, starting from original volumetric data, FEM consists of four sequential steps: (1) image processing; (2) surface mesh generation; (3) volume mesh generation; (4) FEM simulation. Output of each step is the input for the next step.

Original volumetric data is not always applicable for FE modeling because medical images contain noise and artificial effects. Therefore proper processing steps are necessary. The difficulty is to avoid eliminating bone structures during noise removal procedures. In other words, preserving the connectivity of TB micro-architecture is important, especially for MDCT images, which are of low spatial resolution.

In the community of bone study, most studies focus on FEM simulations (18, 19), while little attention is paid on the mesh model. Several studies use basic cubic bricks as the approximation of bone structure model (18, 21, 24). Some others use Marching Cubes for surface mesh generation. Marching Cubes generates surface mesh with bad triangles that is not satisfactory for FEM simulation and therefore relies on post-processing tools. Several studies rely on commercial software for volume rendition, which limits adoption for automation.

In the following sections, a framework of FEM modeling is introduced to generate meshes of high quality. The framework possesses several desirable properties required for FEM simulation: image topology preservation, surface and volume mesh with well-shaped elements. With these properties, the presented framework is also applicable to other types of imaging modalities and various applications. It is also a general tool for FEM modeling in a broader range.

1.4 Outline

In Section 2, a space-variant hysteresis algorithm is introduced for image processing. State-of-the-art algorithms of surface mesh and volume mesh generation are compared in detail

with respect to generating high quality meshes. In Section 3, experiments of mechanical testing are presented and selection of volume of interests (VOI) is presented. In Section 4, mesh quality of two volume mesh methods, reproducibility of FEM predicted bone stiffness on repeat MDCT scans, and correlations of bone stiffness between FEM predicted results and mechanical testing are presented. Finally, in Section 5, a conclusion is drawn and possible applications of the framework is discussed.

CHAPTER TWO

METHODS

In this section, a framework of FEM modeling with sequential steps: (1) image processing, (2) surface mesh generation, (3) volume mesh generation, and (4) FE simulation is presented. Related works are reviewed in each step and advantages and disadvantages of different methods are discussed. The rationale of the framework is also presented and its suitability for FE modeling is shown, especially for MDCT imaging.

2.1 Image Processing

Limited spatial resolution and partial volume effect of MDCT introduce two major challenges for FE modeling. First of all, thin TB structures are lost and remaining TB structures show higher width in MDCT, as shown in Fig. 1. In computer aided design, imaging of higher spatial resolution consumes excessive computational time and memory in FEM simulations especially in large volumes. Although delicate TB structures are sacrificed under low resolution, major branches and topology connections can be preserved under MDCT. It is arguable a trade-off between precision and computational complexity in FEM simulation. Recently, Bauer *et al.* (21) had shown that MDCT-based FEM methods well predicted failure load under spatial resolution of 250μm×250μm×500μm, and argued that such spatial resolution is sufficient for FEM simulation. Here, original MDCT images are obtained in the resolution of 215μm×215μm×200μm. Following the guidance in (25),

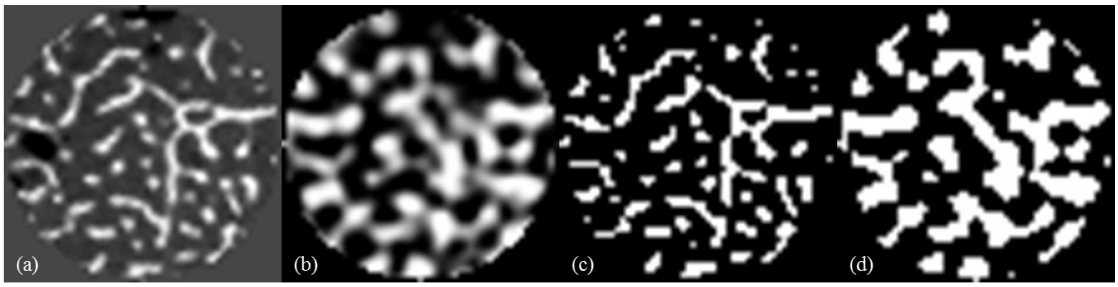

Figure 1. Transverse view of one matching slice of trabecular bone using the same cylindrical VOI. (a) Fuzzy image of μ-CT. (b) Fuzzy image of MDCT. (c) Binary image of μ-CT. (d) Binary image of MDCT.

TB thickness is approximately 150μm. For convenience and consistency with other related TB studies, MDCT images are interpolated into 150μm×150μm×150μm resolution.

Secondly, to get a better approximation of TB architecture, image processing of MDCT is necessary that the image should maintain trabecular structures with preserved connectivity, i.e., holes, tunnels, cavities (26-28). Distance information is often used to preserve structural connectivity (29-33). Here, a space-variant hysteresis approach is presented to maintain trabecular structure and preserve connectivity. The advantage of this method is that it doesn't rely on a fixed threshold to yield binary image. Instead, a hysteresis approach using dynamic thresholds are introduced, enhanced by distance metrics which take bone structure information into consideration.

Distance based hysteresis connectivity.

Given volumetric imaging data $I = \{g(p)|p = (x,y,z), x,y,z \in N\}$, N is a non-negative integer; p is a point on the rectilinear grid; $g(p)$ denotes the intensity value at p. Let $M = \{dist(p)|p \in I\}$ denotes the distance map of I; $dist(p)$ represents the value of distance transform at point p; $dist_{max}$ denotes the maximum value of distance. Map M is computed using Euclidean distance transform.

To generate surface mesh, a binary image I^* is required. However, due to image techniques and noise, delicate bone structures often have low intensity which is comparable to noise. Usually, a single threshold can't distinguish these structures from noise. A high

threshold leads to loss of bone voxels and a low threshold may introduce large amount of noise.

TB closer to the cortical bone are thicker than TB in the core region, and therefore generally have higher intensity and clearer connections. Based on the important observation, an adaptive function is designed to generate dynamic thresholds based on the distance map M:

$$T_1(p) = t_1 + \frac{d_1}{1+e^{-12\left(\frac{M(p)}{dist_{max}}-0.5\right)}} \quad (1)$$

$$T_2(p) = t_2 + \frac{d_2}{1+e^{-12\left(\frac{M(p)}{dist_{max}}-0.5\right)}} \quad (2)$$

Where t_1 and t_2 are two thresholds $(t_1 > t_2)$. $M(p)$ is the distance value at p; d_1 and d_2 are control parameters which determine the variability of the dynamic thresholds. If a voxel p is close to cortical bone, $M(p)$ approximates to 0 and thus (1) and (2) approximate to $t_1 + d_1$ and $t_2 + d_2$, respectively. If p is far from cortical bone, $M(p)$ approximates to 1 and thus (1) and (2) approximate to t_1 and t_2, respectively.

Let I_{s1} denotes a subset of I that represents solid bone voxels; then $I_{s1} = \{g(p)|g(p) \geq T_1(p), p \in I\}$, t_1 is set to a high threshold so that I_{s1} only contains reliable solid bone voxels that can be easily classified by thresholding.

Let I_{s2} denotes a subset of I that also represents bone voxels but with lower intensity (less than $T_1(p)$). Let $Neigh_m(p)$ denote points in the $m \times m$ neighborhood of p. For any point p, if $T_2(p) \leq g(p) < T_1(p)$, and the number of its neighbors that belongs to I_{s1} is larger than a constant c_m, then p is also trusted as a solid bone voxel.

$$I_{s2} = \{g(p)|T_2(p) \leq g(p) < T_1(p), \sum q > c_m, q \in Neigh_m(p), g(q) > T_1(q), p, q \in I\}$$

I_{s2} involves voxels that are in the neighborhood of reliable solid bone voxels whose intensity values are not sufficient high to be easily classified using one fixed threshold.

With I_{s1} and I_{s2} as trusted bone voxels, a hysteresis approach is applied on voxels with lower intensity. Another dynamic threshold is defined as.

$$T_3(p) = t_3 + \frac{d_3}{1+e^{-12\left(\frac{M(p)}{dist_{max}}-0.5\right)}} \quad (3)$$

Where $t_3 < t_2 < t_1$, t_3 is an approximate intensity value that could possibly be a bone voxel or noise. For any voxel p, if $g(p) > t_3$, and p is connected to $Neigh_m(p)$, p is added to I_{s2}. Repeat the hysteresis step until there aren't any such voxels. Finally, the binary image $I^* = I_{s1} \cup I_{s2}$.

The image processing procedure is summarized in Algorithm 1.

Algorithm 1. Distance based hysteresis.

Input: $I, t_1, t_2, t_3, d_1, d_2, d_3, m, c_m$

Output: I^*

1. Calculate distance transform map M from I.
2. $\forall p \in I$, calculate $T_1(p)$, if $g(p) \geq T_1(p)$, add p into I_{s1}.
3. $\forall p \in I - I_{s1}$, calculate $T_2(p)$, if $g(p) \geq T_2(p)$, and $\sum q \geq c_m$, add p into I_{s2}, where $q \in Neigh_m(p) \cap I_{s1}$.
4. Set up an empty queue Q. $\forall p \in I_{s1} \cup I_{s2}$, push p into Q.
5. While Q is not empty:
   Pop top element p from Q.
   $\forall q \in Neigh_m(p) \cap (I - I_{s1} - I_{s2})$, calculate $T_3(p)$.
   If $g(q) \geq T_3(p)$, add q into I_{s2}, push q into Q.
6. $I^* = I_{s1} \cup I_{s2}$.

The space-variant hysteresis approach makes use of dynamic thresholds to classify bone voxels based on their distance to cortical bone. The advantage of dynamic thresholds is that it preserves bone voxels in the region where bone voxels have lower intensity values that traditional one-threshold procedure is not able to classify. In addition, connectivity is also taken into consideration. Therefore, it avoids misclassifying noise which is often isolated, or receives less support of solid bone voxels.

2.2 Surface mesh generation

Given volumetric imaging data I, surface mesh generator produces a mesh representation H_S of the isosurface $S = \{f(p)|f(p) = c, p \in I\}$, where each point on the surface has the

same value c. c is a constant and f is an implicit function. Specifically, in the application for TB surface generation, given the binary image I^*, $S = \{f(p)|p \in I^*\}$.

FEM has rigorous requirements of mesh. With respect to topology and geometry, FEM requires the mesh to be manifold, non-self-intersecting. With respect to sensitivity and precision, FEM relies on mesh quality determined by shape and size of elements. A good mesh generation method should have desired properties which guarantee the topological and geometrical correctness as well as producing elements with high quality.

In computer aided design, triangular mesh is the most common representation of surface mesh. Angles of triangles are therefore the measure of triangular mesh quality. Triangles with small angles are considered as bad elements, for example, a triangle whose smallest angle is less than 1 degree. The sensitivity of FE model is impacted by bad elements of the mesh. In other words, the ability of avoiding bad elements is the key to quality mesh generation.

Surface mesh generation algorithms for FEM are expected to produce elements with good quality that guarantee topology and geometry as well as being timely and computationally efficient. However, it is theoretically difficult for mesh generation algorithms to meet all desired properties. Among various methods for surface meshing in literature, they can be classified into three categories: lattice based method, dual based method, and Delaunay based method. Here, only the most widely used and applicable to FE modeling are reviewed.

Lattice based methods guarantee topology and geometry but fail to generate mesh of good quality. Marching Cubes (34) is the most well-known and widely used method (35). Marching Cubes iterates along the rectilinear grid, classifies each voxel into a predefined case depending on the local information of the voxel and produces triangular surface mesh. The advantage of Marching Cubes is that it is fast, easy for implementation, and generates manifold isosurface. However, the main drawback is that the triangular mesh may include triangles with small angles (less than 0.1 degree), which doesn't meet the

criteria of FEM simulations. Therefore, a post-processing step is often inevitable to smooth the mesh and improve the quality. It requires additional time while the quality of surface mesh may not be guaranteed.

Dual based methods preserve features of the surface and produces triangles with adaptive sizes and thus time and memory efficient. However, these method suffer from non-manifold elements and elements of bad quality. Dual Contouring (DC) (36) introduces the perception of dual grids. Octree is used to represent volumetric data. Therefore sizes of triangles can be controlled by depth of the octree. An edge e with two end points $p, q \in I$ is marked as sign-change edge when $p \in S \; and \; q \notin S$. Whenever a sign-change edge is found, DC creates a dual edge and construct quads using dual edges. It is shown that dual edges could approximate the surface S and preserves sharp features of S by minimizing a quadratic error function. The advantage of DC is that it is adaptive in resolution, computationally efficient and preserves sharp features of the surface. However, the surface mesh generated by the original DC is non-manifold and also ambiguous under certain circumstances. Improved DC (37) addresses the ambiguity but the generated surface mesh is still non-manifold. Similar to the lattice based methods, a post-processing step is necessary to improve quality of generated triangles. Yet, no guarantee of good qualities is ensured while non-manifold situations add difficulty for the post-processing procedure.

Delaunay based methods generate triangles subject to the given surface point set I^* to approximate the topology of the surface, where triangles satisfy the Delaunay criteria. Unlike lattice based and dual based method, Delaunay based methods are not heuristic and are strictly restricted by the Delaunay criteria. Therefore, Delaunay based methods can precisely state properties of the surface and generate surface mesh of good quality. Compared with lattice based and dual based methods, Delaunay based methods require more time and memory. Nevertheless, the ability to generate guaranteed quality mesh makes it suitable for FE calculation. Recently, Boissonnat and Oudot (38) introduce a Restricted Delaunay Triangulation (RDT) algorithm that returns a manifold, non-self-

intersecting, topology preserving triangular surface mesh with provably good triangular quality. RDT iteratively computes Delaunay triangles and adds new points onto the surface to preserve desired properties, i.e., Delaunay criteria and manifold topology. The intersection point of the triangle's dual edge on the corresponding Voronoi Diagram with the surface is added when the radius of triangle's circumsphere is larger than a fraction of the distance from the point to the nearest point on the medial axis. Then the Restricted Delaunay Triangulation is locally updated, after which the manifold topology and Delaunay criteria are both satisfied.

There're two major advantages of the RDT algorithm. First, the algorithm is proved to generate triangular mesh with the smallest angle larger than a user specification as long as it is no larger than 30 degree. The provable bounded angles ensure the availability for further FE calculations. Second, the algorithm eliminates the unnecessary time consuming post-processing step for quality improvement, which is a crucial component for lattice based and dual based methods to get satisfactory surface mesh quality. Besides, the post-processing step often relies on smoothing and is possible to break the correctness of topology and geometry, for example, introducing self-intersections or invert elements.

In the framework, the RDT based method is used as the surface mesh generator because of its desirable properties for FEM simulation. With the help of CGAL (39), surface mesh is generated with provably good mesh quality. The minimum angle is 30 degree and the maximum angle is 150 degree.

2.3 Volume mesh generation

Given surface mesh H_S, volumetric mesh generator produces a polygonal representation H_V of the interior volume of H_S. S_V, the surface of H_V, is an approximation to the isosurface S. Among feasible polygonal representations, tetrahedron is the dominant representation and attracts the most research interests. The equilateral tetrahedron with all dihedral angles equal to $\arccos(1/3) \approx 70.5^{\circ}$, is the ideal high-quality element. Divergence of dihedral angles from the ideal value measures the quality of tetrahedron elements. Specifically,

minimum and maximum dihedral angles of H_V have a great influence on the quality of volume mesh since they slow the convergence and reduce sensitivity of FEM simulations. Aspect ratio is another measurement for mesh quality. It is the ratio of the length of the longest edge over the shortest edge. Ideally, the best aspect ratio is 1 (equilateral tetrahedron). Large aspect ratio indicates the element is thin and ill-shaped.

Over the past two decades, an extensive study on volume mesh generation has been performed (40). Various methods has been proposed to generate volumetric mesh with high-quality tetrahedron elements. These techniques can be classified into four categories: advancing-front-based, octree-based, Delaunay-refinement-based, and lattice-based methods.

Advancing-front-based methods generate tetrahedron elements by inserting Steiner points or elements inside the domain heuristically so that new elements satisfy desired size and shape criteria (41). This technique preserves the input surface and terminates until the whole volume is tetrahedralized. An inevitable and difficult step is merging fronts because of intersections generated during the algorithm. Although advancing-front-based methods are fast, they can't offer any guarantees of mesh quality. As a result, in reality, global smoothing steps are usually required to improve the output quality. Still, mesh quality is not guaranteed and bad elements may exist.

Octree-based methods produces tetrahedron elements of adaptive sizes by controlling the octree depth. It subdivides the domain recursively into cubical cells adaptively according to local grid information. The advantage is that total number of elements of the domain is much less compared with uniform methods. Therefore, it reduces computational time since computation in FEM simulation is determined by number of elements. Several variants are proposed to generate high quality mesh. Shephard *et al.* (42) introduced Finite Octree method which reproduces features of the input surface. Bielak *et al.* (43) presented a parallel method to speed up mesh generation. Mitchell and Vavasis (44) offer octree mesher with theoretical guarantee of avoiding bad tetrahedral by

generalizing the quadtree mesher of Bern *et al.* (45) from two dimension to three dimensions.

Delaunay-refinement-based methods generates tetrahedron elements by inserting points to enforce tetrahedra satisfying constraints on size and quality, as well as maintaining a Delaunay or constrained Delaunay triangulation (46). These methods produce volume mesh with surface exactly the same as the input. Delaunay criteria optimizes the radius to edge ratio but it doesn't guarantee dihedral angles in three dimension. Therefore, slivers, where the tetrahedron element has a good radius to edge ratio but dihedral angles can be arbitrarily between 0 and 180°, may occur, and the near coplanar area of slivers may be over-refined (47). Chew (48) presented an algorithm to eliminate most slivers. Cheng *et al.* (49) presented a technique called sliver exudation that takes as its input a Delaunay triangulation with good radius to edge ratios and returns output mesh without extremely bad slivers. Alliez *et al.* (41) proposed a variational algorithm to generate isotropic tetrahedral mesh and achieved to generate elements with good shape. However, slivers may still survive and there is no guarantee to completely remove them. In practical conditions, these methods usually eliminate most skinny tetrahedron elements and generate satisfactory volume meshes. Tetgen (50) is arguably the most popular mesh generator. It generates exact constrained Delaunay triangulation and boundary conforming meshes by adding Steiner points to control user-specific element size.

Lattice-based methods construct rectilinear grids and generate tetrahedron elements based on pre-computed stencils. Labelle and Shewchuk (51) present a lattice-based algorithm called Isosurface Stuffing (IS) based on body centered cubic (BCC) lattice and prove that the generated volume mesh has bounded dihedral angles guaranteed by the computer-assisted proof. Bounded dihedral angles are between 10.7° and 164.8°. The algorithm works similar to Marching Cubes algorithm except that a point snapping technique is introduced to adjust points on the surface to meet the quality and topology requirement. IS is one of few algorithms that provides theoretical guarantees on dihedral

angles and generated mesh with good quality. Inspired by this method, Doran (52) introduces an algorithm using A15 lattice grid. Wang and Yu (40) propose a robust meshing algorithm based on adaptive BCC lattice grid, offering bounded dihedral angles larger than 10° if uniform mesh is generated and 5.71° in adaptive case. The drawback of these methods is that generated surface mesh is not exactly the same as the input because the point snapping procedure relocates several surface points.

In this work, two most advance methods are compared and their mesh qualities are shown in Section 4. Tetgen is used since it is widely used and arguably the most favorable volume mesh generator for FEM simulation. IS is selected since it is the most recently developed technique for quality mesh generation and one of few guaranteed quality mesh generating algorithm.

CHAPTER THREE

EXPERIMENTS

In this section, the overall experimental plan is presented. biomedical experiment are described in Section 3.1 and 3.2. Then the image acquisition, VOI selection and FE simulation are presented in 3.3, 3.4 and 3.5, respectively.

3.1 Specimen preparation for mechanical testing

Cylindrical TB specimens nominally 8 mm in diameter and 20.9 ± 3.3 mm in length were cored from each distal tibia specimen *in situ* along the proximal-distal direction for mechanical testing. A-P and M-L radiographs were first used to determine the plane of an initial distal cut done to eliminate the growth plate from a test specimen, and then to determine the central axis of the bone and thus the core location; the initial distal cut was located 2 mm proximal to the growth plate. Each specimen was cored with saline immersion using an 8.25 mm inner diameter diamond coring bit (Starlite Industries, Rosemont, PA). The core was released from the distal radius by cutting it with a razor saw, and the specimen ends were sanded smooth, flat, and parallel. Specimen length and diameter were measured three times and averaged, and the middle 6 mm of the specimen length was marked for extensometer attachment position.

3.2 Mechanical testing

Compressive Young's modulus of each TB core was mechanically determined on an electromechanical materials testing machine (MTS Insight, MTS Systems Corp., Eden Prairie, MN). Each specimen was placed between unlubricated, polished, plano-parallel steel platens. To minimize specimen end effects, strain was measured with a 6 mm gage length extensometer (model 632.29F-30, MTS Systems Corp., Eden Prairie, MN) attached directly to the midsection of the bone. A compressive preload of 10 N was applied and strains then set to zero. At a strain rate of 0.005 sec^{-1}, each specimen was preconditioned

to a low strain with at least ten cycles and then loaded to failure. Young's modulus (E) was determined for each specimen as the highest 20% section slope of the stress-strain curve.

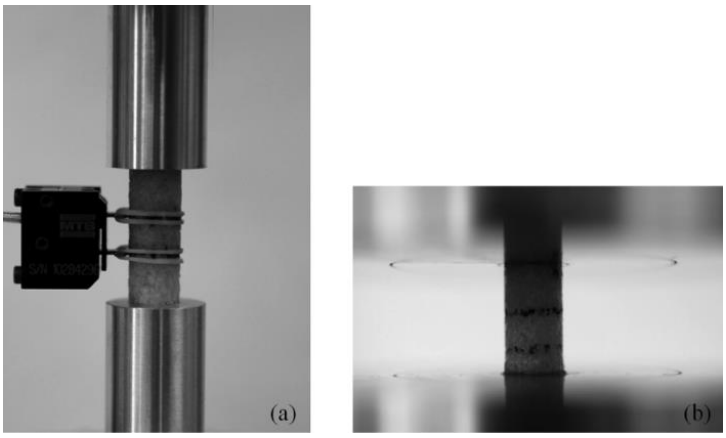

Figure 2. Compressive mechanical testing of trabecular bone specimens. (a) Extensometer testing (b) Trabecular bone specimen after extensometer testing; note black lines indicating central 6mm region for Young's modulus. Proximal and distal part are damaged.

3.3 MDCT imaging

Twenty two fresh-frozen human cadaveric ankle specimens were obtained from 12 body donors (age at death: 82.3±12.5 years). The bodies were collected under the Deeded Bodies Program, The University of Iowa, Iowa City, Iowa, USA, and the ankle specimens were removed at mid-tibia. Exclusion criteria for this study were evidence of previous fracture or knowledge of bone tumor or bone metastasis. The ankle specimens were kept frozen until MD-CT and μ-CT Imaging.

High resolution MD-CT scans of the distal tibia were acquired at the University of Iowa Comprehensive Lung Imaging Center on a 128 slice SOMATOM Definition Flash scanner (Siemens, Munich, Germany) using the following CT parameters: Single tube Spiral acquisition at 120 kV, 200 effective mAs, 1 sec rotation speed, pitch factor: 1.0, nominal collimation: 16x0.3 mm, scan length of 10 cm beginning at the distal tibia end-plateau and total effective dose equivalent:17 mrem ≈ 20 days of environmental radiation in the USA. One AP projection scout scan of the entire tibia was acquired to locate the field of view (FOV) for the CT scan. High resolution MD-CT scan mode: The Siemens Flash

scanner has two 64 rows of equal 0.6 mm detectors under two X-ray guns allowing operation in both single and dual source scan modes. The highest resolution single gun scan mode was used, which activated 16 of the most inner 0.6 detectors to maximize beam quality. Siemens double z sampling allowed for a dual sampling of the 0.6 mm detectors, splitting the signal so that each detector created a 0.3mm slice in the z plane (53). As specified by the manufacturer, the z-UHR scan mode within the Siemens Flash scanner enabled high image detail with a maximum achievable isotropic resolution of 30 lp/cm (0.17 mm) at 0% modulation transfer function (MTF) (± 10 %) and thus provided a more accurate slice profile and lowered partial volume artifact allowing for better separation of TB structures. After scanning each specimen in a helical mode with a 0.4 mm slice thickness, data were reconstructed at 0.2 mm slice thickness using a normal cone beam method with a special U70u kernel achieving high structural resolution. A calibration phantom was scanned once per specimen to calibrate CT Hounsfield units into BMD (mg/cm^3). Three repeat MD-CT scans of each distal tibia specimen were acquired after repositioning the specimen on the CT table before each scan. Following MD-CT repeat scans, each specimen was further scanned on an Imtek Micro-cat II scanner at 28.8µm isotropic resolution, after removing soft tissue and dislocating the tibia from the ankle joint.

3.4 VOI selection

The objective of VOI selection for the cadaveric study was to select a region that is close to the region that was drilled during specimen preparation for mechanical testing. Size and location of these VOIs were chosen as per the information recoded during specimen preparation for each experiment. First, the bone was oriented to align its axis along the coordinate z-axis using the following two steps – (1) generation of a cylinder C with its axis lying on the coordinate z-axis and its cross-sectional area equating the average tibial cross-sectional area, and (2) reorientation of the tibial volume to align its axis with C by maximizing the overlap between the tibial volume and the cylinder C. After reorienting the bone image, a VOI cylinder of 8 mm diameter along the coordinate z-axis was generated

and its proximal end was manually positioned at the center of the cortical rim using in-plane translation through a graphical user interface. The location of the distal end of the

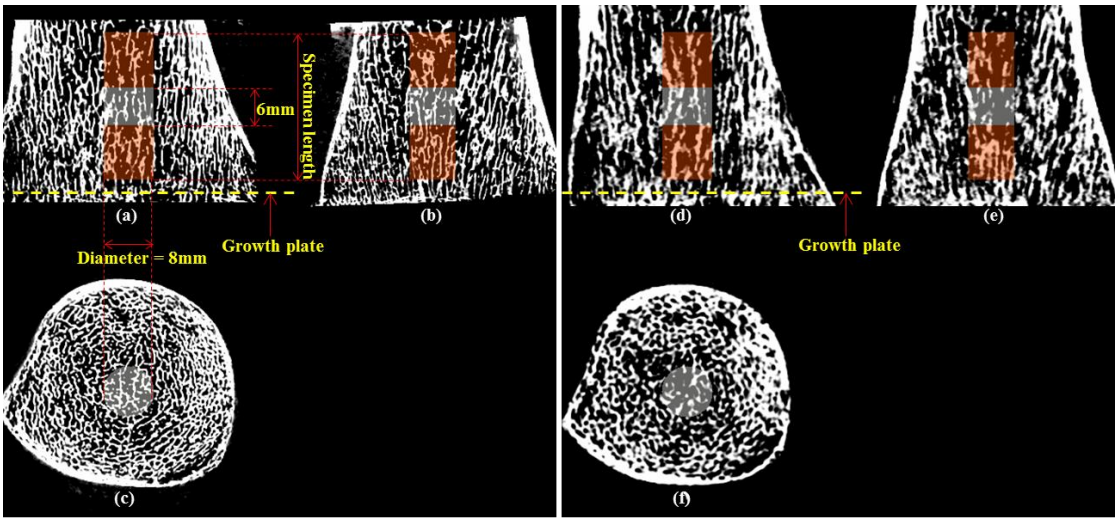

Figure 3. (a), (b), (c) are coronal, sagittal and transverse view of one subject using μ-CT, respectively. The same for (d), (e), (f) but using MDCT. The drilled specimen in mechanical testing is shown in red. The central 6mm is the VOI for the extensometer test

VOI cylinder in the slice direction and its length were determined as per the core location and length recorded during specimen preparation; the growth plate was visually located in the CT data of each specimen. Finally, the central 6 mm region from the cylinder was used as VOI for the extensometer test.

3.5 FE simulation

A linear FE simulation model is applied on the generated volume mesh to compute the Young's modulus of TB. A trabecular subject is modeled as an isotropic, linear elastic material with a Young's modulus of 10 GPa, and a Poisson ratio of 0.3. Abaqus is used as the FE simulator. A uniaxial displacement equaling 2% of the bone segment height was applied perpendicularly to the distal surface of the tibia for determining axial stiffness. Bottom of the cylinder is fixed and constant forces are applied onto the top plane, which simulates the real mechanic testing.

CHAPTER FOUR

RESULT AND DISCUSSION

4.1 Results

4.1.1 Mesh quality

Surface mesh quality is guaranteed by restricted Delaunay Triangulation, the minimum angle is 30 degree and the maximum angle is 150 degree. Generated angles are guaranteed and therefore a post-processing step is no longer necessary.

For the volume mesh quality, aspect ratios and dihedral angles are compared between the IS method and the constrained Delaunay method provided by Tetgen. As shown in Fig. 4(a) and (d), aspect ratios generated by Tetgen mainly fall into [2, 10], which means that the largest edge is no larger than 10 times longer than the shortest edge. The result is satisfactory and extremely large edge ratios don't exist. On the other hand, the IS method generates near ideal tetrahedron elements, and edge ratios are all 1.5. Averaged dihedral angles distribution using the μ-CT and MDCT datasets is shown in Fig. 4. The constrained Delaunay method produces dihedral angles distributed in the range [4.2, 171.5]

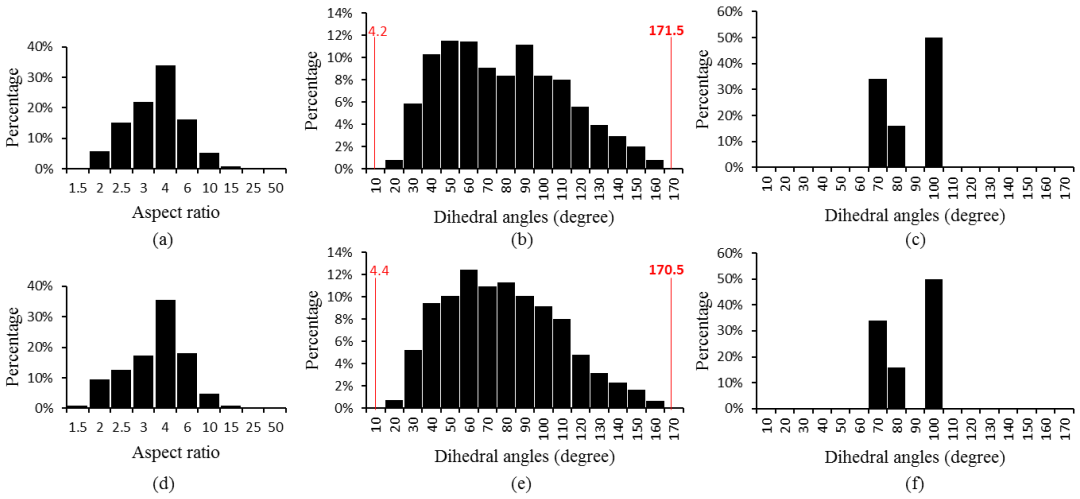

Figure 4. Distribution of aspect ratios generated by Tetgen of μ-CT (a) and MDCT (d). Aspect ratios generated by Isosurface Stuffing are all 1.5. Distributions of dihedral angles generated by Tetgen of μ-CT (b) and MDCT (e). Distribution of dihedral angles generated by Isosurface Stuffing of μ-CT (c) and MDCT (f).

for μ-CT dataset and [4.4, 170.5] for MDCT dataset. Most generated dihedral angles are between 30 and 150 degree, as shown in Fig. 4(b) and Fig. 4(e). Less than 2 percent of dihedral angles are observed either less than 30 degree or larger than 150 degree. Extremely bad dihedral angles don't appear among overall 88 images (including 22 μ-CT images and 66 repeat MDCT images) although the constrained Delaunay method doesn't offer a theoretical guarantee. It confirms that the constrained Delaunay method works well in practice. The IS method generates near ideal tetrahedron elements with good dihedral angles with the help of BCC grid, as shown in Fig. 4(c). For FEM simulation, tetrahedron elements generated by the IS method are preferred. However, the IS method sacrifices surface sensitivity to generate tetrahedron elements with good dihedral angles. Points on the surface are snapped to nearest BCC grid vertices if they are too close, i.e., distance between a point and the corresponding BCC grid vertex is less than a constant $\alpha \in (0,1)$ times the length of the grid. In the volume mesh construction, the element size is controlled no larger than the spatial resolution, therefore, the generated BCC grid is no larger than one voxel size. As a result, snapped points will be dislocated no larger than α times one voxel size. In my experiment, it is considered to be tolerable for the FE simulation. In applications with strict requirement of surface sensitivity, Tetgen is the better choice. In the framework, the IS method is applied as the volume mesh generator for FEM simulation.

4.1.2 Reproducibility

For each cadaveric subject, three repeat scans of MDCT images are obtained. Prior to the image processing and VOI selection, three repeat scans are registered to the μ-CT image. Therefore, the VOI was selected only once for each subject. As shown in Fig. 5, compared with mesh generated using μ-CT, subtle TB structures are missing in meshes generated with MDCT. It is visually seen that meshes of repeat scans of MDCT show high reproducibility. And it is confirmed by the statistical analysis shown in Fig. 6. FE

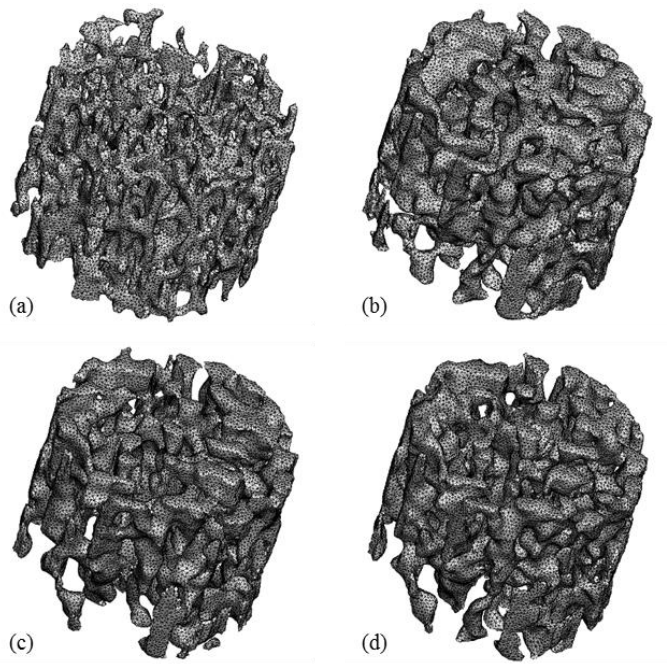

Figure 5. (a) Mesh representation of the cylindrical VOI of a subject using μ-CT. The cylindrical VOI is the central 6mm used in extensometer test. (b), (c), (d) the same as (a) but for different repeat scans using MDCT.

simulation is applied on volume meshes generated by repeat MDCT scans and Young's modules are calculated. The ICC is computed across three repeat scans on 22 subjects. The

ICC value was observed to be 0.98, which indicates that predicted Young's modulus is highly reproducible.

4.1.3 Correlation

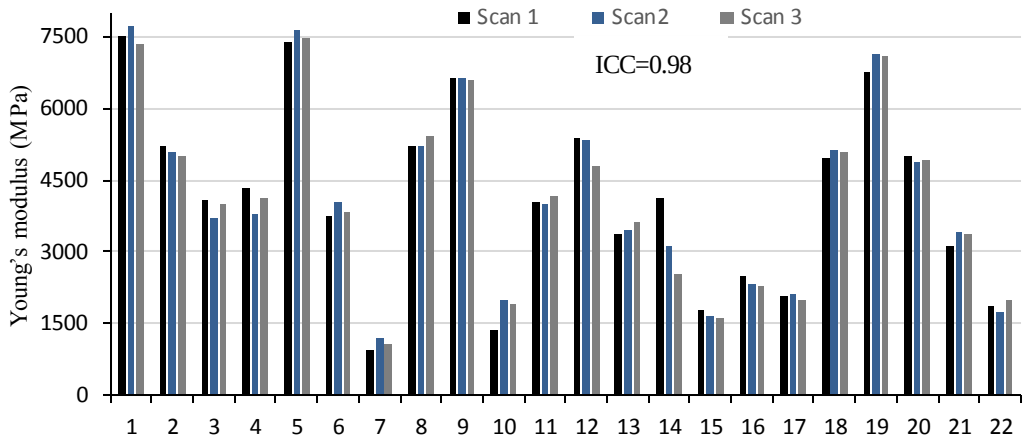

Figure 6. Reproducibility of Young's modulus generated with different MDCT scans. Intra-class correlation coefficient (ICC) is 0.98.

In the last section, it is demonstrated that meshes generated with repeat MDCT scans are highly reproducible. Therefore it is plausible to use the averaged Young's modulus of repeat scans as measure for MDCT. The linear correlation between the averaged Young's modulus and Young's modulus predicted by the μ-CT model is shown in Fig. 7(a). R^2 was found to be 0.87. The averaged Young's modulus predicted by MDCT shows a high correlation with Young's modulus predicted by μ-CT. The result reveals that although MDCT images can't preserve subtle TB structures due to limited spatial resolution, it is capable to approximate the structural stiffness property.

The correlations between predicted Young's modulus by FEM simulation and mechanical testing are shown in Fig. 7(b) and Fig. 7(c). The linear correlation between Young's modulus yielded by μ-CT and mechanical testing was found to be R^2=0.95, which

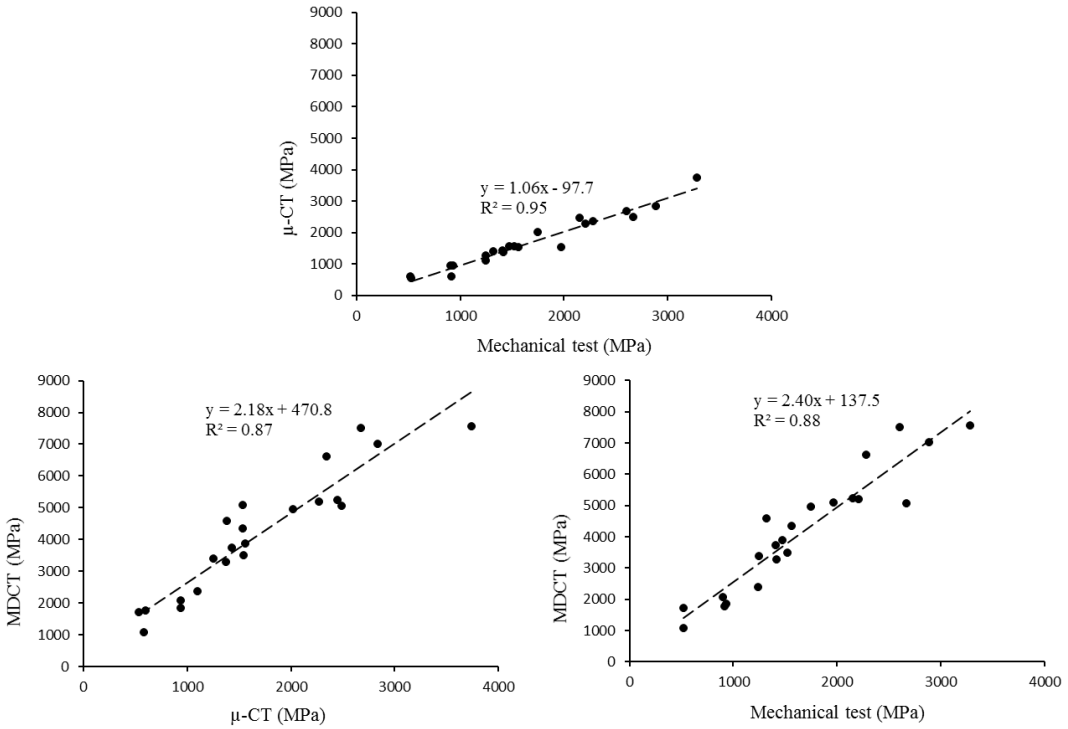

Figure 7. (a) Mesh representation of the cylindrical VOI of a subject using μ-CT. The cylindrical VOI is the central 6mm used in extensometer test. (b), (c), (d) the same as (a) but for different repeat scans using MDCT.

indicates that the FE modeling of μ-CT had successfully predicted the stiffness of the TB. The linear correlation between averaged Young's modulus yielded by MDCT and mechanical testing was found to be R^2=0.88.

4.2 Discussion

Mesh quality generated by two advanced methods have been shown. The method with better tetrahedral quality is selected for the framework. High reproducibility found for yielded Young's modulus across repeat MDCT scans shows that the framework is robust and works well for MDCT images. The high correlation found between predicted Young's

modulus and mechanical testing demonstrates the FEM model is of high sensitivity. The correlation of yielded Young's modulus between MDCT and μ-CT validates the feasibility of applying FE simulation on MDCT. We observed that Young's modulus predicted by MDCT have a constant scaling (2.4) of true values. The reason is two folds. First, subtle architecture of TB is missing under the limited spatial resolution. Second, during the image processing of MDCT, to preserve the connectivity and the completeness of the TB structure, some partial volumes are classified as bone and therefore generated models are thick. However, despite the deficiency of MDCT images, a high correlation is found between predicted Young's modulus by MDCT and mechanical testing. The result suggests that MDCT is able to be used for FE simulation and the framework had successfully predicted the stiffness of TB.

While designed for bone study in MDCT, the framework has a broader range in applications of FEM simulations. Since the framework possesses several desired properties for bone image processing and FEM simulation and had been validated on MDCT, it is expected to be applied on other high-resolution imaging techniques.

CHAPTER FIVE

CONCLUSION

Over the past two decades, FE simulations have been widely used in bone study together with the remarkable progress in high-resolution imaging techniques. However, little attention is paid on the MDCT imaging. Besides, there is an apparent gap between the community of clinical experts and experts of image processing and quality mesh generation. This paper tries to fill the gap with a complete and fully automatic framework of FEM modeling and apply it on MDCT images. It proposes a space-variant hysteresis image processing protocol for bone images. State-of-the-art methods for mesh generation are applied with respect to mesh quality in the framework. Bone stiffness is computed with μ-CT and MDCT using this framework. Actual bone stiffness is determined by mechanical testing. Bone stiffness predicted by FEM were observed to be highly reproducible and correlate well with that of the mechanical testing. The result demonstrates that MDCT is capable to be used for FEM simulation. The framework has been successfully applied on FEM of both μ-CT and MDCT imaging under condition. Currently, the method is investigated on MDCT images from Iowa bone development study and the pilot study data involving subjects from different study groups with expected difference in bone metabolism. The framework is expected to be applied in a broader range on imaging.

REFERENCES

1. Melton, L.J., *How Many Women Have Osteoporosis Now*. J Bone Min Res, 1995. **10**(2): p. 175-177.
2. Looker, A.C., E.S. Orwoll, C.C. Johnston, R.L. Lindsay, H.W. Wahner, W.L. Dunn, M.S. Calvo, T.B. Harris, and S.P. Heyse, *Prevalence of low femoral bone density in older US adults from NHANES III.* J Bone Min Res, 1997. **12**(11): p. 1761-1768.
3. Ammann, P. and R. Rizzoli, *Bone strength and its determinants.* Osteoporos Int, 2003. **14 Suppl 3**: p. S13-18.
4. Wehrli, F.W., P.K. Saha, B.R. Gomberg, H.K. Song, P.J. Snyder, M. Benito, A. Wright, and R. Weening, *Role of magnetic resonance for assessing structure and function of trabecular bone.* Top Magn Reson Imag, 2002. **13**: p. 335-356.
5. Benito, M., B. Vasilic, F.W. Wehrli, B. Bunker, M. Wald, B. Gomberg, A.C. Wright, B. Zemel, A. Cucchiara, and P.J. Snyder, *Effect of testosterone replacement on trabecular architecture in hypogonadal men.* J Bone Miner Res, 2005. **20**(10): p. 1785-91.
6. Chesnut III, C.H., S. Majumdar, D.C. Newitt, A. Shields, J. Van Pelt, E. Laschansky, M. Azria, A. Kriegman, M. Olson, E.F. Eriksen, and L. Mindeholm, *Effects of salmon calcitonin on trabecular microarchitecture as determined by magnetic resonance imaging: results from the QUEST study.* J Bone Miner Res, 2005. **20**(9): p. 1548-1561.
7. Benito, M., B. Gomberg, F.W. Wehrli, R.H. Weening, B. Zemel, A.C. Wright, H.K. Song, A. Cucchiara, and P.J. Snyder, *Deterioration of trabecular architecture in hypogonadal men.* J Clin Endocrinol Metab, 2003. **88**(4): p. 1497-502.
8. Kleerekoper, M., A.R. Villanueva, J. Stanciu, D.S. Rao, and A.M. Parfitt, *The role of three-dimensional trabecular microstructure in the pathogenesis of vertebral compression fractures.* Calc Tiss Int, 1985. **37**: p. 594-597.
9. Legrand, E., D. Chappard, C. Pascaretti, M. Duquenne, S. Krebs, V. Rohmer, M.F. Basle, and M. Audran, *Trabecular bone microarchitecture, bone mineral density and vertebral fractures in male osteoporosis.* J Bone Min Res, 2000. **15**: p. 13-19.
10. Saha, P.K., Y. Xu, H. Duan, A. Heiner, and G. Liang, *Volumetric topological analysis: a novel approach for trabecular bone classification on the continuum between plates and rods.* IEEE Trans Med Imag, 2010. **29**(11): p. 1821-1838.
11. Liu, X.S., P. Sajda, P.K. Saha, F.W. Wehrli, G. Bevill, T.M. Keaveny, and X.E. Guo, *Complete volumetric decomposition of individual trabecular plates and rods and its morphological correlations with anisotropic elastic moduli in human trabecular bone.* J Bone Miner Res, 2008. **23**(2): p. 223-35.
12. Liu, X.S., P. Sajda, P.K. Saha, F.W. Wehrli, and X.E. Guo, *Quantification of the roles of trabecular microarchitecture and trabecular type in determining the elastic modulus of human trabecular bone.* Journal of Bone and Mineral Research, 2006. **21**(10): p. 1608-1617.
13. Majumdar, S., D. Newitt, A. Mathur, D. Osman, A. Gies, E. Chiu, J. Lotz, J. Kinney, and H. Genant, *Magnetic resonance imaging of trabecular bone structure in the distal radius: relationship with X-ray tomographic microscopy and biomechanics.* Osteoporos Int, 1996. **6**(5): p. 376-385.
14. Saha, P.K., B.R. Gomberg, and F.W. Wehrli, *Three-dimensional digital topological characterization of cancellous bone architecture.* Int J Imag Sys Tech, 2000. **11**: p. 81-90.
15. Wald, M.J., B. Vasilic, P.K. Saha, and F.W. Wehrli, *Spatial autocorrelation and mean intercept length analysis of trabecular bone anisotropy applied to in vivo magnetic resonance imaging.* Medical physics, 2007. **34**(3): p. 1110-1120.

16. Morgan, E.F., H.H. Bayraktar, and T.M. Keaveny, *Trabecular bone modulus–density relationships depend on anatomic site*. Journal of biomechanics, 2003. **36**(7): p. 897-904.
17. Van Rietbergen, B., H. Weinans, R. Huiskes, and A. Odgaard, *A new method to determine trabecular bone elastic properties and loading using micromechanical finite-element models*. Journal of biomechanics, 1995. **28**(1): p. 69-81.
18. Zhang, X.H., X.S. Liu, B. Vasilic, F.W. Wehrli, M. Benito, C.S. Rajapakse, P.J. Snyder, and X.E. Guo, *In Vivo μMRI‐Based Finite Element and Morphological Analyses of Tibial Trabecular Bone in Eugonadal and Hypogonadal Men Before and After Testosterone Treatment*. Journal of Bone and Mineral Research, 2008. **23**(9): p. 1426-1434.
19. Boutroy, S., B. Van Rietbergen, E. Sornay‐Rendu, F. Munoz, M.L. Bouxsein, and P.D. Delmas, *Finite element analysis based on in vivo HR‐pQCT images of the distal radius is associated with wrist fracture in postmenopausal women*. Journal of Bone and Mineral Research, 2008. **23**(3): p. 392-399.
20. Jaecques, S., H. Van Oosterwyck, L. Muraru, T. Van Cleynenbreugel, E. De Smet, M. Wevers, I. Naert, and J. Vander Sloten, *Individualised, micro CT-based finite element modelling as a tool for biomechanical analysis related to tissue engineering of bone*. Biomaterials, 2004. **25**(9): p. 1683-1696.
21. Bauer, J.S., I. Sidorenko, D. Mueller, T. Baum, A.S. Issever, F. Eckstein, E.J. Rummeny, T.M. Link, and C.W. Raeth, *Prediction of bone strength by μCT and MDCT-based finite-element-models: How much spatial resolution is needed?* European journal of radiology, 2014. **83**(1): p. e36-e42.
22. Issever, A.S., T.M. Link, M. Kentenich, P. Rogalla, K. Schwieger, M.B. Huber, A.J. Burghardt, S. Majumdar, and G. Diederichs, *Trabecular Bone Structure Analysis in the Osteoporotic Spine Using a Clinical In Vivo Setup for 64‐Slice MDCT Imaging: Comparison to μCT Imaging and μFE Modeling*. Journal of Bone and Mineral Research, 2009. **24**(9): p. 1628-1637.
23. Shewchuk, J., *What is a good linear finite element? interpolation, conditioning, anisotropy, and quality measures (preprint)*. University of California at Berkeley, 2002. **73**.
24. Liu, X.S., A. Cohen, E. Shane, P.T. Yin, E.M. Stein, H. Rogers, S.L. Kokolus, D.J. McMahon, J.M. Lappe, and R.R. Recker, *Bone density, geometry, microstructure, and stiffness: Relationships between peripheral and central skeletal sites assessed by DXA, HR‐pQCT, and cQCT in premenopausal women*. Journal of bone and mineral research, 2010. **25**(10): p. 2229-2238.
25. Saha, P.K. and F.W. Wehrli, *Measurement of trabecular bone thickness in the limited resolution regime of in vivo MRI by fuzzy distance transform*. Medical Imaging, IEEE Transactions on, 2004. **23**(1): p. 53-62.
26. Saha, P.K. and B.B. Chaudhuri, *3D digital topology under binary transformation with applications*. Computer vision and image understanding, 1996. **63**(3): p. 418-429.
27. Saha, P.K., B.B. Chaudhuri, B. Chanda, and D. Dutta Majumder, *Topology preservation in 3D digital space*. Pattern Recognition, 1994. **27**(2): p. 295-300.
28. Saha, P.K. and B.B. Chaudhuri, *Detection of 3-D simple points for topology preserving transformations with application to thinning*. IEEE Trans Pat Anal Mach Intel, 1994. **16**: p. 1028-1032.
29. Saha, P.K., J.K. Udupa, and D. Odhner, *Scale-based fuzzy connected image segmentation: theory, algorithms, and validation*. Computer Vision and Image Understanding, 2000. **77**(2): p. 145-174.
30. Saha, P.K., F.W. Wehrli, and B.R. Gomberg, *Fuzzy distance transform: theory, algorithms, and applications*. Computer Vision and Image Understanding, 2002. **86**(3): p. 171-190.

31. Zhuge, Y., J.K. Udupa, and P.K. Saha, *Vectorial scale-based fuzzy-connected image segmentation*. Computer Vision and Image Understanding, 2006. **101**(3): p. 177-193.
32. Ciesielski, K.C., J.K. Udupa, P.K. Saha, and Y. Zhuge, *Iterative relative fuzzy connectedness for multiple objects with multiple seeds*. Computer Vision and Image Understanding, 2007. **107**(3): p. 160-182.
33. Saha, P.K. and J.K. Udupa. *Iterative relative fuzzy connectedness and object definition: theory, algorithms, and applications in image segmentation*. in *Mathematical Methods in Biomedical Image Analysis, 2000. Proceedings. IEEE Workshop on*. 2000. IEEE.
34. Lorensen, W.E. and H.E. Cline. *Marching cubes: A high resolution 3D surface construction algorithm*. in *ACM Siggraph Computer Graphics*. 1987. ACM.
35. Yu, Z., M.J. Holst, Y. Cheng, and J.A. McCammon, *Feature-preserving adaptive mesh generation for molecular shape modeling and simulation*. Journal of Molecular Graphics and Modelling, 2008. **26**(8): p. 1370-1380.
36. Ju, T., F. Losasso, S. Schaefer, and J. Warren. *Dual contouring of hermite data*. in *ACM Transactions on Graphics (TOG)*. 2002. ACM.
37. Zhang, Y. and J. Qian, *Dual contouring for domains with topology ambiguity*. Computer Methods in Applied Mechanics and Engineering, 2012. **217**: p. 34-45.
38. Boissonnat, J.-D. and S. Oudot, *Provably good sampling and meshing of surfaces*. Graphical Models, 2005. **67**(5): p. 405-451.
39. Rajapakse, C.S., J.F. Magland, and F.W. Wehrli, *Fast prospective registration of in vivo MR images of trabecular bone microstructure in longitudinal studies*. Magn Reson Med, 2008. **59**(5): p. 1120-6.
40. Wang, J. and Z. Yu, *Feature-sensitive tetrahedral mesh generation with guaranteed quality*. Computer-Aided Design, 2012. **44**(5): p. 400-412.
41. Alliez, P., D. Cohen-Steiner, M. Yvinec, and M. Desbrun. *Variational tetrahedral meshing*. in *ACM Transactions on Graphics (TOG)*. 2005. ACM.
42. Shephard, M.S. and M.K. Georges, *Automatic three - dimensional mesh generation by the finite octree technique*. International Journal for Numerical methods in engineering, 1991. **32**(4): p. 709-749.
43. Bielak, J., O. Ghattas, and E. Kim, *Parallel octree-based finite element method for large-scale earthquake ground motion simulation*. Computer Modeling in Engineering and Sciences, 2005. **10**(2): p. 99.
44. Mitchell, S.A. and S.A. Vavasis. *Quality mesh generation in three dimensions*. in *Proceedings of the eighth annual symposium on Computational geometry*. 1992. ACM.
45. Bern, M., D. Eppstein, and J. Gilbert, *Provably good mesh generation*. Journal of Computer and System Sciences, 1994. **48**(3): p. 384-409.
46. Shewchuk, J.R., *Delaunay refinement algorithms for triangular mesh generation*. Computational geometry, 2002. **22**(1): p. 21-74.
47. Cheng, S.-W., T.K. Dey, and J. Shewchuk, *Delaunay mesh generation*. 2012: CRC Press.
48. Chew, L.P. *Guaranteed-quality delaunay meshing in 3d (short version)*. in *Proceedings of the thirteenth annual symposium on Computational geometry*. 1997. ACM.
49. Cheng, S.-W., T.K. Dey, H. Edelsbrunner, M.A. Facello, and S.-H. Teng, *Silver exudation*. Journal of the ACM (JACM), 2000. **47**(5): p. 883-904.
50. Si, H. and A. TetGen, *A quality tetrahedral mesh generator and three-dimensional delaunay triangulator*. Weierstrass Institute for Applied Analysis and Stochastic, Berlin, Germany, 2006.
51. Labelle, F. and J.R. Shewchuk. *Isosurface stuffing: fast tetrahedral meshes with good dihedral angles*. in *ACM Transactions on Graphics (TOG)*. 2007. ACM.

52. Doran, C., A. Chang, and R. Bridson. *Isosurface stuffing improved: acute lattices and feature matching*. in *ACM SIGGRAPH 2013 Talks*. 2013. ACM.
53. Flohr, T., K. Stierstorfer, R. Raupach, S. Ulzheimer, and H. Bruder. *Performance evaluation of a 64-slice CT system with z-flying focal spot*. in *RöFo-Fortschritte auf dem Gebiet der Röntgenstrahlen und der bildgebenden Verfahren*. 2004. © Georg Thieme Verlag KG Stuttgart· New York.